# The Role of $Cu_1$-$O_3$ Species in Single-Atom Cu Catalyst for Directional Methanol Synthesis from $CO_2$ Hydrogenation

**Huibo Zhao**
Fuzhou University
**Ruofan Yu**
Fuzhou University
**Sicong Ma**
Fudan University https://orcid.org/0000-0001-5894-5910
**Yang Chen**
Fuzhou University
**Kaizhuang Xu**
Fuzhou University
**Yuan Fang**
Fuzhou University
**Caixia Zhu**
Fuzhou University
**Xiaochen Liu**
Fuzhou University
**Yu Tang**
University of Kansas https://orcid.org/0000-0001-9435-9310
**LiZhi Wu**
Fuzhou University
**Yingquan Wu**
Institute of Coal Chemistry, Chinese Academy of Sciences
**Qike Jiang**
Dalian Institute of Chemical Physics
**Peng He**
National Energy Research Center for Clean Fuels, Synfuels China Co.
**Zhipan Liu**
Fudan University https://orcid.org/0000-0002-2906-5217
**Li Tan** ( tan@fzu.edu.cn )
Fuzhou University https://orcid.org/0000-0003-4648-3362

**Article**

**Keywords:** Cu-based catalyst, Cu1-O3 units, methanol synthesis

**Posted Date:** July 16th, 2021

**DOI:** https://doi.org/10.21203/rs.3.rs-701447/v1



**Version of Record:** A version of this preprint was published at Nature Catalysis on September 15th, 2022.
See the published version at https://doi.org/10.1038/s41929-022-00840-0.

# Abstract

Cu-based catalysts have attracted much interest in $CO_2$ hydrogenation to methanol because of their high activity. However, the effect of interface, coordination structure, particle size and other underlying factors existed in heterogeneous catalysts render to complex active sites on its surface, therefore it is difficult to study the real active sites for methanol synthesis. Here, we report a novel Cu-based catalyst with isolated Cu active sites ($Cu_1$-$O_3$ units) for highly selective hydrogenating $CO_2$ to methanol at low temperature (100% selectivity for methanol at 180 $^oC$). Experimental and theoretical results reveal that the single-atom Cu-Zr catalyst with $Cu_1$-$O_3$ units is only contributed to synthesize methanol at 180 $^oC$, but the Cu clusters or nanoparticles with Cu-Cu or Cu-O-Cu active sites will promote the process of reverse water gas shift (RWGS) side reaction to form undesirable byproducts CO. Furthermore, the $Cu_1$-$O_3$ units with tetrahedral structure could gradually migrate to the catalyst surface for accelerating $CO_2$ hydrogenation reaction during catalytic process. The high activity isolated Cu-based catalyst with legible structure will be helpful to understand the real active sites of Cu-based catalysts for methanol synthesis from $CO_2$ hydrogenation, thereby guiding further design the Cu catalyst with high performance to meet the industrial demand, at the same time as extending the horizontal of single atom catalyst for application in the thermal catalytic process of $CO_2$ hydrogenation.


# Introduction

The excessive use of fossil fuels in recent decades has led to a dramatic increase in the amount of $CO_2$ in the air, which has caused serious damage to the natural environment. Hence, the related C1 chemistry has become an important research area because one of the most challenging scientific issues is to find alternative energy sources for petroleum in the 21st century [1]. Especially, the conversion of excess $CO_2$ into high value-added chemicals and energy fuels in industry can not only effectively mitigate the greenhouse effect, but also realize the sustainable use of resources by closing the natural carbon ring[2–6]. Methanol ($CH_3OH$), as a basic industrial raw material, can be used to synthesize a series of important industrial chemicals such as low-carbon Olefins and gasoline by means of MTO and MTG[7–12]. It is obvious that the process of $CH_3OH$ catalysis from $CO_2$ is of great commercial value. Therefore, in the past few decades, a lot of research work has been studied to find catalysts with good performance, including metal-metal oxides ($Cu/ZnO/Al_2O_3$[13,14], $Cu/In_2O_3$[15], $Cu/ZrO_2$[16–18], $Pd/ZnO$[19] and so on), metal oxide solid solutions ($ZnO/ZrO_2$[20], $In_2O_3/ZrO_2$[21] and $CdZrO_x$[22]) and metal alloys ($Ni_xGa_y$[23], $Pd_xGa_y$[24], $Pt_xCo_y$[25], etc.)

Cu catalyst has attracted much attention because of its excellent catalytic activity and stability to $CH_3OH$ synthesis among the $CO_2$ hydrogenation catalysts[18,26]. However, Cu-based heterogeneous catalyst is difficult to have a clear understanding of the active sites due to its complex microstructure and various effects between the metal and the support. The diversity of valence states of Cu and the particularity of hydrogenation reactions make Cu mostly exist in mixed valence states during the reaction. It is confused

that the previous literatures show that $Cu^0$, $Cu^+$ or $Cu^{\delta+}$ may be active sites[27–29]. Moreover, the physical size of Cu nanoparticles also profoundly affects the catalytic performance[17,30–32]. Taking $Cu/ZrO_2$ catalyst as an example, Witoon etc.[33] found that the $Cu/ZrO_2$ catalyst with amorphous phase is favorable for methanol synthesis, but Samson etc.[16] claimed that the $Cu/ZrO_2$ catalyst with tetragonal phase has the best catalytic activity in methanol synthesis; Ma etc.[18] believed Cu-Zr interface played a crucial role for methanol synthesis from $CO_3$*→HCOO*→$CH_3O$* route via stabilizing the activated $Cu^+$, but Lercher etc.[32] thought Cu-O-Zr could only activate $CO_2$ to synthesize CO rather than methanol. Although substantial progress has been made in the active sites of Cu catalysts, there are still many controversies on the structure-performance correlation between catalyst and reaction.

Single-atom catalyst is an ideal model for active site study due to its possessed uniform metal sites which is embodied in the homogeneous catalyst[34–36]. However, the related work is rarely reported because it is difficult to construct the effective active sites in the thermal catalytic hydrogenation of $CO_2$ to $CH_3OH$[37–39]. Here, an efficient $Cu_1/ZrO_2$ single-atom catalyst is synthesized to realize the reaction of $CO_2$ hydrogenation to $CH_3OH$ at relatively low temperature (180 $^oC$). Compared to the typical $Cu/ZrO_2$ catalysts, monoatomic dispersed $Cu_1/ZrO_2$ displayed highest $TOF_{MeOH}$ and 100% $CH_3OH$ selectivity. Based on the above catalytic model, the relationship between Cu active sites structure and the formation of methanol or CO is in depth exploration.

# Results

**The design of various type $Cu/ZrO_2$ catalysts with different coordination structure models.** A series of $Cu/ZrO_2$ catalysts with different Cu loading (1–20 wt%) were synthesized by modified co-precipitation method. And the Cu-based amorphous/monoclinic $ZrO_2$ with different Cu amount (x wt%) were named as CAZ-x and CMZ-x, respectively. The actual Cu concentration in various $Cu/ZrO_2$ samples were measured by Inductively Coupled Plasma Optical Emission Spectrometry (ICP-OES) (Table S1). As shown in Figure S1a, all the $Cu/a\text{-}ZrO_2$ catalysts with different Cu loading amount exhibited amorphous state of $ZrO_2$ and no XRD peaks of CuO species, suggesting that the Cu species were highly dispersed on $a\text{-}ZrO_2$[33]. Similar specific surface areas and pore structures also indicated a high degree of dispersion of Cu species (Table S2). Notably, the amorphous $ZrO_2$ transformed to tetragonal phase without adding $Cu^{2+}$ precursor during the same co-precipitation procedure (Figure S1b). The changed phases indicated that strong interaction effect was existed between Cu and $ZrO_2$. The broad peak at $523cm^{-1}$ also confirmed the amorphous zirconia were formed in different Cu loading $Cu/a\text{-}ZrO_2$ catalysts from the Raman spectroscopy (Figure S2)[40].

To confirm the hyperfine structure of the $Cu/a\text{-}ZrO_2$ catalysts at the atomic scale, high angle dark field scanning transmission electron microscope images (HAADF-STEM) and X-ray absorption fine structure (XAFS) spectroscopy were used. The HAADF-STEM images (Fig. 1a, Figure S3) of CAZ-1 showed that the

amorphous state $ZrO_2$ occupied the sample with no Cu nanoparticles on it. The elements mapping (Fig. 1d) and $N_2O$ titration test (Table S3) also confirmed the highly dispersed Cu sites were located in the CAZ-1 catalyst consistent with the XRD and TEM results. With Cu loading amounts increasing to 15 wt%, the Cu species still kept in a highly dispersed state even though a small amount of Cu particles were started to form on the $ZrO_2$ substrate (Fig. 1b and Figure S4). Extended x-ray absorption fine structure spectroscopy (EXAFS) in R space and corresponding WT spectra results could supply more important information about the catalysts structure, as shown in Fig. 1 (g, h) and Figure S5 (a, b). Only one apparent peak at 1.92 Å corresponding to the first coordination shell of Cu-O scattering could be detected in CAZ-1 and CAZ-15 catalysts (Table S4). It evidenced that Cu sites were atomically dispersed in CAZ-1 and CAZ-15 since no Cu-O-Cu or Cu-Cu bond was observed[41]. It was hardly to totally exclude the Cu single atoms via just increasing the Cu loading amount in CAZ-x catalysts due to its unique molecular interactions between Cu and amorphous $ZrO_2$. Therefore, the catalyst with Cu nanoparticles was synthesized over monoclinic $ZrO_2$ substrate with 15wt% Cu amount, named CMZ-15 as reference catalyst. The obvious peaks at 35.5° and 38.7° in XRD (Figure S6a) and at 291 $cm^{-1}$ in Raman spectroscopy (Figure S2) were corresponded to the existence of CuO nanoparticles[42]. The highly agglomerated CuO particles (15–20 nm) were also observed in the CMZ-15 catalyst from the results of TEM (Fig. 1c, Figure S7), elements mapping (Fig. 1f, Figure S7) and $N_2O$ titration (Table S3). Moreover, an additional smaller peak corresponding to CuO at 2.81 Å was observed in EXAFS and WT spectra (Fig. 1g, Figure S5b), ascribed to Cu-(O)-Cu scattering at second shell, confirming the formation of CuO particles[43]. Thus, the three catalysts with different models of single atoms Cu, coexisted single atoms/clusters/nanoparticles Cu and large nanoparticles Cu were built up in CAZ-1, CAZ-15 and CMZ-15, respectively.

**Catalytic performance for $CO_2$ hydrogenation on various $Cu/ZrO_2$ catalysts.** The catalytic performance of $Cu/ZrO_2$ catalysts for $CO_2$ hydrogenation to $CH_3OH$ were evaluated at 180 $^oC$ and 3MPa with $CO_2/H_2$ mixed gas ($CO_2/H_{2=}$1:3). Prior to reaction, all $Cu/a\text{-}ZrO_2$ catalysts were pretreated at 230 $^oC$ for 10 hours under Ar atmosphere. Moreover, CAZ-1, CMZ-15 and CS-15 (mean 15 wt% $Cu/SiO_2$) were pretreated at 250–370°C under $H_2$ atmosphere in order to form Cu particle species, respectively. The $CO_2$ conversion over all the catalysts was controlled less than 10% to study their intrinsic activity, which was far beneath its $CO_2$ equilibrium conversion at this condition (29.7% at 180 $^oC$, Figure S8). As shown in Fig. 2(a, b) and Table S5, only $CH_3OH$ could be detected without any other byproducts over CAZ-1 catalyst and it preferentially produced $CH_3OH$ with a $TOF_{Cu}$ value up to 1.37$h^{-1}$. Therefore, a “homogeneous” active site catalyst with excellent stability was synthesized for $CH_3OH$ production from $CO_2$ hydrogenation. However, $CO_2$ could not be activated in CAZ-1-r (refer to CAZ-1 pre-reduced by $H_2$ at 370°C to form Cu large particles), CMZ-15 and CS-15, where the Cu species were almost entirely composed of large metallic Cu particles, confirmed by XRD (Figure S6a, b, Figure S9) and $H_2$-TPR (Figure S10). Therefore, the highly dispersed isolated Cu species might be the real active sites for the $CH_3OH$ synthesis from $CO_2$ at low temperature. As the Cu amount increased in the CAZ-x catalysts (Fig. 2c), the CO started to be produced from CAZ-4 catalyst, indicating additional active sites were formed in these high Cu loading amount

catalysts (Figure S11). It is inferred that the formed Cu clusters of small nanoparticles on CAZ-x catalyst (> 4 wt% Cu) played a crucial role in accelerating reverse water gas shift reaction (RWGS) since it was no activity over CAZ-1-r, CMZ-15 and CS-15 catalysts with large metallic Cu particles. It was found that the catalysts exhibited excellent intrinsic activity in the low loading range (< 2 wt% Cu). It showed an approximately linear growth relationship of $CO_2$ conversion between CAZ-1 and CAZ-2 with only $CH_3OH$ produced (the ratio of $CO_2$ Conv. CAZ-2/CAZ-1 and Cu amount CAZ-2/CAZ-1 is 0.96), indicating that all Cu active sites were uniformly dispersed and exposed on the catalysts surface. However, the increasing trend of conversion rate decreased as the Cu amount higher than 4 wt% (The ratio of $CO_2$ Conv. CAZ-4/CAZ-1 and Cu amount CAZ-4/CAZ-1 is 0.67), since the Cu clusters or small nanoparticles could not provide $CO_2$ activation ability as strong as isolated Cu active sites, thereby the CO selectivity was much lower than $CH_3OH$ selectivity. When the Cu loading amount was more than 8 wt%, the surface of the catalyst was filled up with Cu clusters and isolated Cu sites, at the same time as Cu large particles without $CO_2$ activation ability being gradually formed (Figure S12), resulting in no further increase of the $CO_2$ conversion due to the saturation of surface active sites.

The conclusion was also evidenced by the catalytic performance and ICP-OES results (Table S1) of the CAZ-15-H catalyst (H: $HNO_3$ pre-treated), where the large Cu nanoparticles were partially removed. The catalytic performance was almost similar to that of CAZ-8 ~ 20 and the actual Cu loading amount was close to that of CAZ-8, indicating that the serviceably effective active sites of Cu species on a-$ZrO_2$ surface were about 7 ~ 8 wt%. Meanwhile, it was proved that the active sites in the catalyst were in a very stable structure, even strong acid could not break its structure. The CAZ-1 catalyst was also conducted in $CO_2$ conversion reaction for continuous 100 h to evaluate its catalytic stability (Fig. 2d, Figure S13). After the induction period for a couple of hours, the catalyst with isolated Cu active sites gave both very stable $CO_2$ conversion and target products selectivity during this period, which revealed that the catalyst possessed an extremely steady structure in the $CO_2$ hydrogenation reaction, Furthermore, fresh and used CAZ-1 catalysts had similar weight loss and heat absorption/exothermic trend, which indicated that CAZ-1 catalyst had stable structure and no carbon deposition on its surface during low-temperature reaction (Figure S14).

**Surface electronic state and coordination structure.** The catalysts electronic state and the coordination environment in the short range were investigated to study the relationships to their catalytic performance. The X-ray photoelectron spectroscopy (XPS) and X-ray near-edge structure spectroscopy (XANES) results were shown in Fig. 3. In comparison to the CAZ-15, the absence of Cu 2p satellite peaks between 940eV and 945eV implied that no $Cu^{2+}$ species exited in the fresh and used CAZ-1 catalysts[15,44]. Identical peaks situated at 932.9eV between $Cu^0$(932.4eV) and $Cu^{2+}$(934.6eV) were observed in CAZ-1 and CAZ-1-U (U: used), indicating the Cu species were at cationic $Cu^{\delta+}$ state[31,45]. The position of Cu $2p_{3/2}$ was not shifted after the reaction, giving another strong evidence that the active $Cu^{\delta+}$ species was very stable in the CAZ-1 catalyst, at the same time as no metallic Cu nanoparticles forming to make sure supplying enough stable active sites in $CO_2$ hydrogenation process (Fig. 2d and S13). Moreover, the peak of Cu $L_3M_{45}M_{45}$

Auger centred at 915.5eV without any shifting in CAZ-1 and CAZ-1-U also confirmed the stable $Cu^{\delta+}$ species in catalyst surface (Figure S15)[31]. However, the satellite peaks of Cu $2p_{3/2}$ that appeared in CAZ-15, suggesting that $Cu^{2+}$ species were formed in CuO clusters or nanoparticles (Fig. 3a)[46]. After the $CO_2$ hydrogenation reaction, the weakening of the satellite peak intensity and the shifting of Cu 2p3/2 from 933.6eV to low binding energy (932.5eV ~ Cu0) indicated that the $Cu^{2+}$ was partially in-situ reduced to $Cu^0$ at CAZ-15 during the reaction[45,47]. The XAES results also proved the valence state of Cu partially changed after reaction in CAZ-15 catalyst (Figure S15). Therefore, the unstable surface structure led to its relatively poor $CH_3OH$ selectivity. The co-existed $Cu^0$ and $Cu^{\delta+}$ species in CAZ-15 would convert $CO_2$ to CO and $CH_3OH$, respectively. The chemical states of Cu species were also investigated by XANES (Fig. 3b). The weak pre-edge peak located at 8977-8978eV (1s→3d) and 8984eV(1s→4p) suggested that the Cu species were exited in the form of cationic state in CAZ-1 and CAZ-15, which was a little similar to the CuO with tetrahedral structure[41,48,49]. However, compared to the CuO, the obvious “step” of the pre-edge peak located at ~ 8984eV(1s→4p) disappeared since the tetrahedral structure was highly asymmetric according to its unsaturated coordination state. Meanwhile, it was inferred that the Cu species in the bulk structure of the CAZ-15 catalyst were also highly dispersed, but the different surface Cu state led to its different catalytic performance in $CO_2$ hydrogenation. The apparent pre-edge peak at 8984eV was detected in CMZ-15, which confirmed that CuO particle was embodied in CMZ-15[49]. The EXAFS fitting data for $Cu/ZrO_2$ were shown in Fig. 3c, Figure S16 and Table S4, suggesting the local structure of CAZ-1 was composed of one isolated Cu atom coordinated with ~ three oxygen atoms ($Cu_1$-$O_3$ unit) in a tetrahedral geometric configuration with defects. The stable isolated $Cu_1$-$O_3$ units rather than Cu-(O)-Cu in CAZ-15 were the real active sites for $CH_3OH$ synthesis from $CO_2$.

**The active sites for $Cu/ZrO_2$ catalysts.** It was supposed that isolated $Cu_1$-$O_3$ sites might be favor of $CO_2$ directional converting to $CH_3OH$. Because no Cu particles were detected in used CAZ-1(Fig. 4a and Figure S17a), which confirmed that isolated $Cu_1$-$O_3$ active sites in $Cu/ZrO_2$ were really stable. However, the local Cu particles with 0.21nm spacing for Cu (111) planes[15,48,50,51] detected in used CAZ-15 by HRTEM (Fig. 4b, Figure S17b) revealed that Cu species were partially aggregated and reduced during the catalytic process, consistent with the XPS results (Fig. 3a and Figure S15). $H_2$-TPR was also tested to understand the evolution of the Cu species under reduced atmosphere (Figure S10). The $Cu^{\delta+}$ species in CAZ-1 were hard to be reduced because only one peak at 360°C was appeared, which was much higher than actual reaction temperature, indicating the stability of $Cu_1$-$O_3$ active sites. As the Cu content increased from 1 wt% to 15 wt%, the reduction peak shifted to lower temperature, demonstrating that the interaction between the Cu species and $ZrO_2$ carrier became weak gradually. The reason was the Cu species would be more easily aggregated thereby further reduced as its loading amount increasing. It was also supported by XRD results (Fig. 4c, Figure S12) that no Cu particle diffraction peaks were detected and the crystal structure still kept in amorphous state for the used CAZ-1 catalyst. In contrast, two obvious sharp peaks (43.3° and 50.4°) [52,53]were appeared in used CMZ-15, suggesting the formation of Cu from CuO reduction (Figure S6). Furthermore, in-situ XRD was employed to investigate the dynamic evolution of

$Cu^{\delta+}$ species in Cu/a-$ZrO_2$ under $H_2$ atmosphere. As shown in Fig. 4d, no signal of $Cu^0$ was observed in CAZ-1 catalyst with temperature increasing (30→180→230→300→350 $^oC$). On the contrary, for the CAZ-15, two faint signals at 43.3$^o$ and 50.4$^o$ appeared and the intensity gradually enhanced during the process of temperature increasing from 180 $^oC$ to 350 $^oC$ at $H_2$ atmosphere. Therefore, the $Cu^{2+}$ species in CAZ-15 were partial reduced at 180 $^oC$ and high temperature could further accelerate the reduction state. In the $H_2$-TPD test (Figure S18), the peak at ~ 420 $^oC$ were assigned to the $H_2$ absorbed sites at Cu species and a-$ZrO_2$ substrate. Compared with CAZ-1, the peak at ~ 420 $^oC$ in CAZ-15 migrated to a higher temperature (415 $^oC$ → 430 $^oC$), possibly caused by the more supplied adsorption sites on CAZ-15 surface, indicating that the structure of Cu species in CAZ-15 was more complex and non-unique. Based on above results, it is concluded that the dispersion of Cu species in CAZ-1 were still in single-atom state; Cu single-atom with partially reduced clusters or nanoparticles were coexisted in CAZ-15 during the reaction. As for CMZ-15, both XRD (Figure S6) and $H_2$-TPR (Figure S10) results indicated that almost all Cu species were reduced to larger Cu particles during the reaction.

While Cu loading amount was less than 2 wt% in CAZ-x catalysts, the only product was $CH_3OH$ since the isolated $Cu_1$-$O_3$ unit played the crucial role for $CH_3OH$ synthesis (Fig. 2c). As the Cu loading amount was increased to 4 wt%, a small amount of CO was produced, because a small number of reduced Cu clusters or nanoparticles were formed during the reaction (Figure S11), which might be the active sites for RWGS reaction. By increasing the Cu content to 8 wt%, the proportion of CO in the products was also raised due to the more formed Cu clusters or small nanoparticles. In result, all the evidence suggested that single-atom Cu species with isolated $Cu_1$-$O_3$ unit and Cu clusters or small nanoparticles was the active sites for generating $CH_3OH$ and CO, respectively. However, it was found that when the Cu loading amount was further increased to 12 wt%, 15 wt% and 20 wt%, the $CO_2$ conversion and products distribution did not change any more. Because large particles of Cu would be formed as the Cu content further increased, but large particles of Cu had no ability to activate $CO_2$ in low temperature, consistent with the reaction results under CMZ-15 and CS-15 catalysts (Fig. 2). Besides, more clearly Cu lattice fringe in HAADF-STEM (Fig. 4b), more obvious Cu bulk structure in XRD (Fig. 4c), and the Cu reduction peak with lower temperature in $H_2$-TPR (Figure S10) together claimed that more Cu particles were generated by reducing $Cu^{2+}$ species over the CAZ-15 during the reaction.

**Cu $^{\delta+}$ species migration during the reaction.** Capturing the evolution of active metal species during the reaction is very essential for the in-depth understanding of the active site, especially in reactions involving hydrogen. A number of studies have shown that the gases in the pretreatment or reaction process greatly affect the structure of catalysts, including active species migration and surface reconstruction[54–56]. A similar effect also existed in our Cu/$ZrO_2$ catalyst system, where $H_2$ promoted the migration of $Cu^{\delta+}$ species to the surface of support. Time of Flight Secondary Ion Mass Spectrometry (TOF-SIMS) was an extremely sensitive method to analyze the dispersion of elements at the catalyst surface, where located at 1–3 atomic layers on the surface of catalyst can be detected (Fig. 5a, b). More bright red spots were

detected in Fig. 5b, suggesting more Cu species appeared at the surface in used CAZ-1 catalyst. Semi-Quantitative analysis of the surface Cu (Fig. 5c) also displayed that the surface of used CAZ-1 catalyst contained more Cu species, which indicated that Cu species would migrate to the surface during the reaction. Same results were also supported by XPS analysis (Figure S19), the intensity of $Cu_{2p}$ spectra for the used CAZ-1, CAZ-15 were much stronger than fresh catalysts respectively, which meant Cu species were getting enriched on used catalyst surface after the reaction. Meanwhile, Cu/Zr ratio calculated by XPS further confirmed the above conclusion. The surface Cu/Zr ratios of CAZ-1 and CAZ-15 samples were 0.0012 and 0.24, and the corresponding ratios for used $Cu/ZrO_2$ catalysts were 0.0018 and 0.38, respectively. Obviously, there were more Cu active sites on the catalysts surface appeared after reaction. Moreover, in-situ DRIFT was used to verify the Cu migration as well and supply another important evidence. The catalysts were adsorbed to saturation in CO atmosphere before the desorption experiment was carried out with Argon. The absorbed peak at 2102$cm^{-1}$ was assigned to linear adsorption of CO on the Cu species (Figure S20a, b) [42,57]. For the fresh catalyst, the CO concentration decreased rapidly with the Ar purge time, and the surface residual concentration was close to zero at 20 min. In comparison, the desorption rate of CO on the used CAZ-1 was much slower than that on the fresh catalyst, at the same time as the obvious CO signal being still observed after 20 min gas purging. For more intuitive comparison, it was normalized the area of the CO absorption peak at 2102 $cm^{-1}$ and made a time-dependent surface concentration attenuation spectrum with the Ar purging time (Figure S20c). It was also concluded that the quantity of CO absorption on used CAZ-1 was much more than that on the fresh catalyst, which proved that the surface of the used catalyst contains more Cu sites.

Based on the above facts of Cu migration, it was inferred that the dynamic change of $Cu_1$-$O_3$ active sites during the reaction process. EXAFS data have shown that the Cu species in $Cu/a\text{-}ZrO_2$ were mainly single-atom dispersed in the fresh catalyst, and the Cu species would migrate to the surface at a certain rate under the induction of reaction gas. That was the reason of the reaction had a certain induction period at initial hours (Fig. 2d, S13). It was concluded that the unique $Cu_1$-$O_3$ structure in CAZ-1 was vital for $CH_3OH$ synthesis at the low temperature. The Cu sites in CAZ-1 remained Cu single-atom with isolated $Cu_1$-$O_3$ structure after migrating to the surface due to the small amount of Cu. However, more Cu sites in CAZ-15 were accumulated and in-situ reduced during migration in hydrogen atmosphere process (Fig. 4c-d). Therefore, the migration behavior of Cu species during the reaction could be divided into three types according to the catalytic activity results: 1. When Cu content was less than 2 wt%, the migrated Cu species were not accumulated during the reaction process and the Cu species still distributed in mono-dispersed state, hence only $CH_3OH$ was produced and $CO_2$ conversion was enhanced with the increasing Cu loading amount in linear; 2. When the Cu loading amount was between 4–8 wt%, the Cu species were migrated to the surface for partly agglomeration, and the activity showed that the $CO_2$ conversion and CO selectivity was increased while the $CH_3OH$ selectivity was decreased due to the formed Cu clusters or small nanoparticles producing CO via RWGS; 3. When the Cu loading amount was higher than 8 wt%, the partial Cu species would be kept aggregating to form large Cu particles without $CO_2$ activation ability,

thus the conversion of $CO_2$ and the products distribution were not changed any more. The schematic diagram was shown in Fig. 5d.

**The reaction mechanism of $CO_2$ hydrogenation on $Cu/ZrO_2$ catalysts.** To clarify the structure influence for absorbed species on the surface, in-situ diffuse reflectance Fourier transform infrared spectroscopy analysis was carried out at reaction situation. All the tests were performed at 180 $^oC$ and the assignments of all band vibration peaks were listed in Table S6. As shown in Fig. 6a for CAZ-1, the active species were mainly first exited in $HCO_3^*$; the peaks located at 1695$cm^{-1}$, 1431$cm^{-1}$ were assigned to bicarbonate species, i-$HCO_3^*$ and 1631$cm^{-1}$, 1226$cm^{-1}$ were $\nu_{as}$ ($HCO_3$), $\nu_s$ ($HCO_3$) of b-$HCO_3^*$[58], respectively. As the reaction proceeded, the $HCO_3$* were slowly transformed into formate species, according to the peaks at 1595$cm^{-1}$, 1384$cm^{-1}$, 1371$cm^{-1}$, 2736$cm^{-1}$, 2877$cm^{-1}$ and 2970$cm^{-1}$ which were attributed to $\nu_{as}$ (OCO), δ (CH), $\nu_s$ (OCO), δ (CH) + $\nu_{as}$ (OCO), $\nu$ (CH) and δ (CH) + $\nu_s$ (OCO)[59–62]. In fact, the transform of bicarbonates to formate may underwent the path of $HCO_3^* \rightarrow CO_2 \rightarrow HCOO^*$. The $H_2$ was also necessary because no evolution of $HCO_3^*$ to $HCOO^*$ can be detected in CAZ-1 by only absorbed $CO_2$ (Figure S21). Meanwhile, the vibration peaks at 1072$cm^{-1}$, 1146$cm^{-1}$, 2827$cm^{-1}$ and 2935$cm^{-1}$ for $CH_3O$* were also discovered, which could be assigned to $\nu$ (CO)-terminal, $\nu$ (CO)-bridge, $\nu_s$ ($CH_3$) and $\nu_{as}$ ($CH_3$)[59,60,62]. Therefore, the process of $CO_2$ hydrogenation to $CH_3OH$ in CAZ-1 was followed the formate path. Furthermore, it was proved that the $CH_3OH$ was not produced from the in-situ CO hydrogenation via the RWGS route at initial according to the reaction results of showing no catalytic activity over CAZ-1 in CO hydrogenation process under same reaction condition (Table S5). For CAZ-15 catalyst, the $CH_3OH$ signal located at 1007$cm^{-1}$ was detected during the in-situ DRIFT test[61], which indicated the process of $CH_3OH$ formation was greatly promoted on CAZ-15 due to possessing more definitely quantity of active sites for $CH_3OH$ synthesis (Figure S22). In fact, the $CO_2$ adsorption capacity of the catalysts was not significantly changed by only enhancing the loading amount of Cu species, because CAZ-1 and CAZ-15 had similar adsorption mode and adsorption amount for $CO_2$ (3.0mmol/$g_{cat}$ in CAZ-1, 2.9mmol/$g_{cat}$ in CAZ-15, Figure S23). It was concluded that the increase of methanol production rate was not affected by the adsorption capacity in these two catalysts, but mainly caused by the different active sites numbers. As increasing Cu loading amount to 15 wt%, the absorption of intermediate species on the surface of CAZ-15 was much more complex than that on CAZ-1. In addition to the adsorbed bicarbonate (1621$cm^{-1}$, 1225$cm^{-1}$), carbonate (1247$cm^{-1}$, 1324$cm^{-1}$, 1455$cm^{-1}$) formate (1360$cm^{-1}$, 1384$cm^{-1}$, 2864$cm^{-1}$, 2974$cm^{-1}$) and methoxy species (1070$cm^{-1}$, 1146$cm^{-1}$, 2836$cm^{-1}$, 2921$cm^{-1}$), the carboxylate signals were also captured at 1287$cm^{-1}$ and 1756$cm^{-1}$ [63]. The $CH_3OH$ was formed by accompanied with the reverse water gas shift reaction since more complex Cu active sites (single-atom, cluster and particle) were provided under reaction, leading to the decrease of $CH_3OH$ selectivity. As for CMZ-15 with Cu large nanoparticles (Figure S24), all the absorbed species were $CO_3^*$ or $HCO_3^*$ but no further hydrogenation intermediates were observed, demonstrating that the Cu large nanoparticles could not realize the further hydrogenation of carbonate at low temperature, which was corresponded to the results of activity test.

Based on the above information, intensity-time shift spectra supplied the dynamic behavior of intermediates converting on CAZ-1 and CAZ-15 in the reaction (Fig. 6b). The peaks at 2877$cm^{-1}$, 2935$cm^{-1}$ in CAZ-1 and 2866 $cm^{-1}$, 2921$cm^{-1}$ in CAZ-15 were chosen to study the dynamic evolution of $CH_3O^*$ and $HCOO^*$ under reaction condition (180 $^oC$, 3 MPa). The ratio of $HCOO^*/CH_3O^*$ increased over both CAZ-1 and CAZ-15 catalysts with reaction time extended, which indicated that the transformation process of HCOO* to $CH_3O$* was the rate-limiting step compared to the $HCOO^*$ generating process in the $CH_3OH$ synthesis from $CO_2$. Furthermore, the $HCOO^*/CH_3O^*$ increase rate of CAZ-15 was much slower than CAZ-1, which suggested that the consumption of $HCOO^*$ species would be faster on the surface of CAZ-15. Considering the relative rates of $HCOO^*$ formation and its further converting to $CH_3O^*$ were the same for each $Cu_1$-$O_3$ site in producing methanol over CAZ-1 and CAZ-15. The only reason to explain the different $HCOO^*/CH_3O^*$ increase rate over these two catalysts was resulted from CAZ-15 contained more different types of Cu active sites for HCOO* conversion, such as HCOO*-–CO.

The excellent selectivity to $CH_3OH$ of CAZ-1 could be attributed to its unique $Cu_1$-$O_3$ catalytic center as confirmed by DFT calculations. Figure 7 and Figure S(25, 26) showed the calculated lowest energy pathway for $CO_2$ hydrogenation, which involved $HCOO^*$, $H_2COO^*$ and $CH_3O^*$ key intermediates. The reaction started from the dissociative adsorption of $H_2$ molecule on a Cu-O pair to form Cu-H and OH groups, which was exothermic of 0.44 eV. At reaction temperature (180 $^oC$), the adsorption became thermoneutral due to the entropy losses. The dissociation energy barrier of $H_2$ is 0.71 eV. $CO_2$ molecule adsorbed physically near the Cu-H group with the free energy change being 0.58 eV. While there were two possible channels for $CO_2$ hydrogenation, i.e., to $HCOO^*$ or to $COOH^*$, our calculations showed that the formation of $COOH^*$ group had a high barrier of 0.78 eV (Figure S27), but the formation of $HCOO^*$ was barrierless (0.01 eV). Thermodynamically, the $COOH^*$ group was also 0.63 eV less stable than the $HCOO^*$ group. The formed $HCOO^*$ adopted a bidentate configuration with two O ends linking with the Zr and Cu atoms with the distance being 2.22 and 1.94 Å, respectively. This indicated that $HCOO^*$ pathway was the only viable route for $CO_2$ hydrogenation.

After $HCOO^*$ formation, a second $H_2$ molecule came to dissociate on the Cu and the neighboring two-coordinated surface O with endothermic energy of 0.22 eV. The C atom of $HCOO^*$ group could then be hydrogenated to $CH_2OO^*$ group with a barrier of 0.66 eV and the reaction was almost thermoneutral (endothermic by 0.07 eV). After that, $CH_2OO^*$ could easily pick up the left H to form $CH_2OOH^*$ with only 0.07 eV barrier. In $CH_2OOH^*$, the hydroxyl oxygen bonded with the Cu atom with the bond length of 2.3 Å. It could further break the C-O bond to form $CH_2O^*$ and hydroxyl groups by overcoming a barrier of 0.62 eV. The generated $CH_2O^*$, being a saturated molecule, preferred to bond with surface Zr atom, resulting in the re-exposure of Cu site that allowed the dissociative adsorption of the third $H_2$. The dissociated H atom on Cu site could spontaneously react with the neighboring hydroxyl group to form a water molecule (exothermic by 0.31 eV) that could desorb readily. The $CH_2O^*$ could stepwisely reacted with neighboring H

atoms to form $CH_3O^*$ and $CH_3OH^*$. The reaction barriers for these two hydrogenation steps were 0.01 and 1.06 eV with the reaction energies being − 0.48 and 1.06 eV, respectively. The desorption of $CH_3OH$ would further release 0.62 eV energy.

It should be mentioned that the identified $HCOO^*$ and $CH_3O^*$ intermediates were consistent with the in-situ spectroscopy from experiment. The rate determining step in the pathway was the $CH_3O^*$ hydrogenation to $CH_3OH^*$ that has a barrier of 1.06 eV. The data also agreed reasonably with the barrier (~ 1.15 eV) deduced from the experiment TOF (1.3 $s^{-1}$) for CAZ-1 based on microkinetics.

Based on the above research results, we established the reaction model diagram for $CO_2$ hydrogenation over the CAZ-x series catalysts. As shown in Fig. 8, when the Cu species were distributed in a single atom level with uniform $Cu_1$-$O_3$ catalytic centers on the surface of $ZrO_2$, $CO_2$ would convert to methanol with 100% selectivity. When the Cu species were existed in the form of clusters or small nanoparticles, $CO_2$ could only produce CO. As the Cu species were in larger particles, there was almost no catalytic effect for activating $CO_2$. Therefore, it was believed that the $Cu_1$-$O_3$ sites in Cu single atoms and Cu clusters/small nanoparticles were the catalytic active sites for methanol and CO synthesis from $CO_2$ hydrogenation, respectively, while the larger Cu particles were not the active sites for $CO_2$ hydrogenation at this condition.

# Conclusions

This work reveals the influence of different Cu structure models on $CO_2$ hydrogenation process. The unsaturated coordination $Cu_1$-$O_3$ species is favorable for generating $HCOO^*$, which is a vital intermediate during the $CH_3OH$ synthesis. It is also proved that $HCOO^*$ pathway is the only viable route for $CO_2$ hydrogenation. Moreover, the hydrogen is more easily dissociated and further hydrogenated in the Cu atom with its adjacent O atoms. Therefore, the isolated $Cu_1$-$O_3$ active sites contained in Cu single-atom catalyst realizes the directional selective of $CO_2$ to $CH_3OH$ (100%) at 180 $^oC$, at the same time as migrating dynamically to the catalyst surface with stable structure during the catalysis process. The Cu clusters and/or small nanoparticles is the active sites for CO formation via the RWGS route. By contrast, the Cu large particles cannot activate $CO_2$ in the low temperature at all. The Cu single-atom catalyst with clear geometry and uniform active site structure provides guidance for further understanding of the Cu active center in $CO_2$ hydrogenation to $CH_3OH$ reaction, at the same time as extending the horizontal of single atom catalyst for application in the thermal catalytic process of $CO_2$ hydrogenation.

# Methods

**Synthesis of CAZ-1.** CAZ-1 was synthesized by modified co-precipitation with $Na_2CO_3$ as precipitant. Firstly, weighing $Cu(NO_3)_2{\cdot}3H_2O$ (Sigma-Aldrich, 98%-103%) and $Zr(NO_3)_4{\cdot}5H_2O$ (Macklin, AR) precursors according to the metal loading and dissolved them together into 100ml deionized water to make a 0.03M solution, which was recorded as solution A. Then it was weighed an appropriate amount of $Na_2CO_3$ and

dissolved it in 100ml deionized water to make a 0.06M solution, which was marked as solution B. After the dissolution completed, a peristaltic pump was used to slowly drip the two solutions A and B into another beaker containing 100ml of deionized water at a rate of 0.3ml/min. During the dropping process, the stirring maintained at 350 rpm/min and heated at 80°C until the dropping was completed. Then stopped stirring and aged at 80°C for 2h. After aging, cooled it to room temperature and washed with deionized water to pH=7, followed by drying in an oven at 80°C overnight. Finally, it was ground into powder and calcined in a muffle furnace at 2°C/min to 350°C for 5h.

**Catalyst characterization.** The Cu actual loading in different catalysts was determined by inductively coupled plasma optical emission spectroscopy (ICP-OES) which performed on an iCAP 7000 SERIES (Themo Fisher). The test method was as follows: 10mg sample was dissolved in mix solution (2ml $HNO_3$+6ml HCl+2ml HF) overnight, then add to 50ml volumetric flask and diluted to scale line. Four internal Cu concentration standard solutions (1ppm, 10ppm, 50ppm, 100ppm) were analyzed and formed a standard curve ($R^2$>0.9999) before tested all samples. X-ray diffraction (XRD) was performed on a Japan Rigaku X-Ray diffractometer equipped with graphite monochromatized Cu Kα radiation. Scan angle:10-90°, scan speed: 2°/min, voltage and current: 40kV, 40mA. The Raman spectroscopy data were collected at Themo Fisher DXR2xi with 532nm light source. In-situ XRD was carried out at Rigaku Ultima 4 X-ray diffractometer with Cu Ka radiation (40 kV, 40 mA) in the range of 10-80°C and scanning step length of 0.33 under $H_2$ (30ml/min) atmosphere. The curves were record at room temperature, 180°C, 230°C, 300°C, 350°C, respectively. The morphology and elemental mapping of catalysts were performed on a JEM ARM200F thermal-field emission microscope with a probe spherical aberration (Cs) corrector working at 200 kV and transmission electron microscopy (TEM, FEI Talos F200S G2 at 200kV). TPR curves of samples were collected by Micromeritics Pulse Chemisorb 2705. He (30ml/min) pretreated the sample at 250°C for 2h in order to remove the moisture on the surface. Then 10% $H_2$/He was passed into the reactor with the temperature rise of 10 °C/min to 250°C and recorded data every 0.5 minute. The $N_2O$ titration analysis for measuring surface area and dispersion of metallic Cu were also performed on Micromeritics Pulse Chemisorb 2705. The sample was first reduced by $H_2$ at 300°C and after that cool to room temperature, then pure $N_2O$ (30ml/min) was passed though the sample for 10min. Continue to heat up to 400 $^oC$ and recorded the second TPR peak. The $H_2$ consumption were used to calculate the amount of oxygen deposited after $N_2O$ titration[64]. 1.46 x $10^{19}$ Cu atoms per square metre of surface and a stoichiometry of 2Cu/$H_2$ were used. The $Cu^0$ surface was calculated by the relationship below:

$$SA_{Cu}=6.4955\times10^{-2}\times C\times D$$

Where C, D represent of Cu constant (%) and dispersion, respectively.

XPS and AES data were collected on a ESCALAB 250 photoelectron spectroscope (Thermo Fisher Scientific) which was equipped with monochromatic Al Kα radiation (200 W, E=1486.6eV). The binding energy of all samples was calibrated to C 1s peak at 284.8eV.

X-ray absorption spectroscopy (XAS) test for Cu Kedge (8900-9400eV) was performed at the BL14W1 beamline of the Shanghai Synchrotron Radiation Facility (SSRF) which in transmission mode with the Si (111) monochromator. The data of EXAFS processing were done by Athena/Artemis software packages, based on FEFF 6. Bond length (ΔR), Debye-Waller factor ($\sigma^2$), amplitude factor ($S0_2$) and energy shift ($\Delta E_0$) were used to optimize the fitting results.

DRIFT-CO chemisorption was carried on – (Thermo Fisher Scientific) with MCT detector and Harrick reaction cell. The sample was first treated in Ar (30ml/min) atmosphere at 300 °C for 30min, then cooled to 30°C for background collection. After that 10%CO/Ar was passed through the sample until the adsorption is saturated, then cut off the 10%CO/Ar gas and recorded the desorption spectrum by 32 scans at a resolution of $4cm^{-1}$ under the Ar purge. Operando DRIFT at high pressure (3MPa) was measured on a FT-IR spectrometer (Bruker Vertex 70) with MCT detector and Harrick cell. The samples were first pretreated by He 230°C or $H_2$ at 250°C for 60min, then cool to 150°C and passed in $CO_2/H_2/Ar$ (24/72/4) or $CO_2$ alone. After the pressure reached to 3MPa the background was collected. At last, raised the temperature to 180°C and record the spectrum with absorb time.

Time of Flight Secondary Ion Mass Spectrometry (TOF-SIMS) was test on a PHI nano TOF II Time-of-Flight SIMS which $Bi_3^+$ as ion species. The Energy, ion current, Raster size, Mass range, Mode and Analysis time for test were 30keV, 2nA, 100um×100um, 0-1850u, high mass resolution mode and 5min, respectively.

**Catalytic evaluation.** The catalytic performance of all catalysts was tested on a high-pressure, continuous-flow, fixed bed reactor built by Xiamen Better Works Engineering. 500mg CAZ-x catalysts (40-60 mesh) mixed with 2g quartz sand (40-60 mesh) were pretreated in Ar atmosphere at 230 °C (CAZ-1-r was reduced by $H_2$ at 370°C) in the flow of 30ml/min for 10h. As for CMZ-15 and CS-15, both of them were pretreat by $H_2$ at 250 °C in the flow of 30ml/min for 10h. After the temperature was cooled to 180 °C, $CO_2/H_2/Ar$ (24/72/4) was introduced to a pressure of 3MPa. After the pressure and temperature stabilized, the reacted gas flow was changed to 10ml/min and Shimadzu chromatography equipped with a flame ionization detector (FID) and a thermal conductivity detector (TCD) was used to analyze products online every 30 minutes. The catalytic performance of catalysts was evaluated by $CO_2$ conversion, product selectivity, space-time-yield (STY) and turnover frequency (TOF). The computational formula as follow:

$$(1)\ C_{CO_2} = \frac{X_{CO_2,in} - X_{CO_2,out}}{X_{CO_2},in} \cdot 100\%$$

$C_{CO2}$-Conversion of $CO_2$, %; $X_{CO2,\,in}$-mole fraction of $CO_2$ in pristine mixed gas; $X_{CO2,\,out}$-mole fraction of $CO_2$ in exit gas.

$$(2)\ Sel_{CO} = \frac{X_{CO,out}}{X_{CO_2,in} - X_{CO_{2,out}}} \cdot 100\%$$

Selco-Selectivity of CO, %.

$$(3)\ Sel_i = \frac{R_i f_{i,m}}{\sum_i R_i f_{i,m}} \cdot 100\%$$

$Sel_i$-Selectivity of component *i*,%;

$R_{i,s}$-Area ratio of hydrocarbon in chromatogram;

$F_{i,m}$-Correction of mass.

$$(4)\ TOF_{MeOH} = \frac{F_{CO_2,in} \cdot C_{CO_2} \cdot Sel_{CO_2} \cdot N_a}{W_{cat} \cdot L_{Cu} \cdot D_{Cu} \cdot N_a} \cdot 100\%$$

$TOF_{MeOH}$($h^{-1}$)-Turnover frequency for methanol formation;

$F_{CO2}$(mol/s)-The molar flow rate of $CO_2$;

Na-Avogadro's constant(6.022x1023$mol^{-1}$);

$W_{cat}$(g)-Catalyst weight;

$L_{Cu}$-actual loading of Cu;

$D_{Cu}$ -dispersion of Cu.

$$(5)\ STY_{(MeOH,mmolMeOH \cdot h^{-1} \cdot g_{cat}^{-1})} = \frac{F_{CO_2,in} \cdot X_{CO_2} \cdot S_{MeOH}}{W_{cat}} \cdot 100\%$$

$STY_{MeOH}$-Methanol space-time yield.

**DFT calculations.** All DFT calculations are performed by using the plane wave VASP code[65], where electron-ion interaction is represented by the projector augmented wave pesudopotential[66,67]. The exchange functional utilized is the spin-polarized GGA-PBE[68].11 The kinetic energy cutoff is set as 450 eV. The first Brillion zone k-point sampling utilizes the 1 × 1 × 1 gamma-centred mesh grid. The energy and force criterion for convergence of the electron density and structure optimization are set at 10-5 eV and 0.05 eV/Å, respectively. The detail for calculate mode is showed as follow.

**SSW-NN simulation.** Our approach for resolving complex oxide structures is based on the recently-developed SSW-NN method as implemented in LASP code,[69] where the SSW-NN can achieve the fast global PES exploration. The machine learning NN potential is generated by iterative self-learning of the plane wave density functional theory (DFT) global PES dataset generated from SSW exploration. At present, the SSW-NN method has been successfully applied in solving the structures of oxide,[12,70] zeolite,[71] molecule crystals.[72] The SSW-NN simulation to explore PES can be divided into three steps: global dataset generation based on DFT calculations using selected structures from SSW simulation, NN potential fitting and SSW global optimization using NN potential. These steps are iteratively performed until the NN potential is transferable and robust enough to describe the global PES. The procedure is briefly summarized below.

At first, the global dataset is built iteratively during the self-learning of NN potential. The initial data of the global dataset comes from the DFT-based SSW simulation and all the other data is taken from NN-based SSW PES exploration. In order to cover all the likely compositions of CuZrOH, SSW simulations have been carried out for different structures (including bulk, layer and cluster), compositions and atom number per unit cell. Overall, these SSW simulations generate more than $10^7$ structures on PES. The final global dataset that is computed from high accuracy DFT calculation contains 60,271 structures, which is detailed in Supplementary Table S7.

Then, the NN potential is generated using the method as introduced in our previous work.[73,74] To pursue a high accuracy for PES, we have adopted a large set of power-type structure descriptors, which contains 324 descriptors for every element, including 148 2-body, 170 3-body, 6 4-body descriptors, and compatibly, the network utilized is also large involving two-hidden layers (324-50-50-1 net), equivalent to 75,000 network parameters in total. The min-max scaling is utilized to normalization the training data sets. Hyperbolic tangent activation functions are used for the hidden layers, while a linear transformation is applied to the output layer of all networks. The limited-memory Broyden-Fletcher-Goldfarb-Shanno (L-BFGS) method is used to minimize the loss function to match DFT energy, force and stress. The final energy and force criterions of the root mean square errors are around 6.0 meV/atom and 0.151 eV/Å respectively.

To obtain a reasonable model of $Cu_{SAC}$ on amorphous $ZrO_2$, SSW-NN method is applied to exhaustively search the phase space of $Cu_1O_1/ZrO_2$. The model builds as follows:

(i) From the most stable monoclinic $ZrO_2$ bulk phase, the most stable (-111) surface with (4 × 4) supercell and three $ZrO_2$-layers thickness is built which contains 144 atoms (48 $ZrO_2$ formula unit).

(ii) Then three $ZrO_2$ formula units (9 atoms) is artificially removed from the m-$ZrO_2$ (-111) surface, forming the locally amorphous structure.

(iii) One CuO formula unit (2 atoms) is randomly added around the amorphous $ZrO_2$.

(iv) Starting from this initial model, more than 10000 minima are visited by SSW-NN simulation. From that, the most stable structure of $Cu_1O_1$ on amorphous $ZrO_2$ is obtained with a special $CuO_3$ tetrahedron configuration with the Cu-O bond distances of 1.814, 1.920 and 1.921 Å (Figure S28) which is well consistent with the EXAFS results. This model is verified by plane wave DFT calculations and then adopted for the $CO_2$ hydrogenation reaction.

# References


1 Li, J. et al. Integrated tuneable synthesis of liquid fuels via Fischer–Tropsch technology. *Nat. Catal.* **1**, 787-793 (2018).

2 Jenkinson, D. S., Adams, D. E. & Wild, A. Model estimates of $CO_2$ emissions from soil in response to global warming. *Nature* **351**, 304-306 (1991).

3 Kang, X. et al. Highly efficient electrochemical reduction of $CO_2$ to $CH_4$ in an ionic liquid using a metal–organic framework cathode. *Chem. Sci* **7**, 266-273 (2016).

4 Zhong, J. et al. State of the art and perspectives in heterogeneous catalysis of $CO_2$ hydrogenation to methanol. *Chem. Soc. Rev.* **49**, 1385-1413 (2020).

5 Yao, B. et al. Transforming carbon dioxide into jet fuel using an organic combustion-synthesized Fe-Mn-K catalyst. *Nat. Commun.* **11**, 6395 (2020).

6 Hu, J. et al. Sulfur vacancy-rich $MoS_2$ as a catalyst for the hydrogenation of $CO_2$ to methanol. *Nat. Catal.* **4**, 242-250 (2021).

7 Ferri, P. et al. Chemical and Structural Parameter Connecting Cavity Architecture, Confined Hydrocarbon Pool Species, and MTO Product Selectivity in Small-Pore Cage-Based Zeolites. *ACS Catal.* **9**, 11542-11551 (2019).

8 Ilias, S. & Bhan, A. Mechanism of the Catalytic Conversion of Methanol to Hydrocarbons. *ACS Catal.* **3**, 18-31 (2013).

9 Tan, L. et al. Bifunctional Capsule Catalyst of $Al_2O_3$@Cu with Strengthened Dehydration Reaction Field for Direct Synthesis of Dimethyl Ether from Syngas. *Ind. Eng. Chem. Res.* **58**, 22905-22911 (2019).

10 Tan, L. et al. Design of a core–shell catalyst: an effective strategy for suppressing side reactions in syngas for direct selective conversion to light olefins. *Chem. Sci.* **11**, 4097-4105 (2020).

11 Tan, L. et al. Direct $CO_2$ hydrogenation to light olefins by suppressing CO by-product formation. *Fuel Process. Technol.* **196**, 106174 (2019).

12 Ma, S., Huang, S.-D. & Liu, Z.-P. Dynamic coordination of cations and catalytic selectivity on zinc–chromium oxide alloys during syngas conversion. *Nat. Catal.* **2**, 671-677 (2019).

13 Behrens, M. et al. The Active Site of Methanol Synthesis over $Cu/ZnO/Al_2O_3$ Industrial Catalysts. *Science* **336**, 893-897 (2012).

14 Beck, A. et al. Following the structure of copper-zinc-alumina across the pressure gap in carbon dioxide hydrogenation. *Nat. Catal.* **4**, 488-497 (2021).

15 Shi, Z. et al. $CO_2$ hydrogenation to methanol over Cu-In intermetallic catalysts: Effect of reduction temperature. *J Catal* **379**, 78-89 (2019).

16 Samson, K. et al. Influence of $ZrO_2$ Structure and Copper Electronic State on Activity of $Cu/ZrO_2$ Catalysts in Methanol Synthesis from $CO_2$. *ACS Catal.* **4**, 3730-3741 (2014).

17 Li, K. & Chen, J. G. $CO_2$ Hydrogenation to Methanol over $ZrO_2$-Containing Catalysts: Insights into $ZrO_2$ Induced Synergy. *ACS Catal.* **9**, 7840-7861 (2019).

18 Wu, C. et al. Inverse $ZrO_2/Cu$ as a highly efficient methanol synthesis catalyst from $CO_2$ hydrogenation. *Nat. Commun.* **11**, 5767 (2020).

19 Bahruji, H. et al. Pd/ZnO catalysts for direct $CO_2$ hydrogenation to methanol. *J Catal* **343**, 133-146 (2016).

20 Wang, J. et al. A highly selective and stable $ZnO\text{-}ZrO_2$ solid solution catalyst for $CO_2$ hydrogenation to methanol. *Sci. Adv.* **3**, e1701290 (2017).

21 Martin, O. et al. Indium Oxide as a Superior Catalyst for Methanol Synthesis by $CO_2$ Hydrogenation. *Angew. Chem. Int. Ed.* **55**, 6261-6265 (2016).

22 Wang, J. et al. High-Performance MaZrOx (Ma = Cd, Ga) Solid-Solution Catalysts for $CO_2$ Hydrogenation to Methanol. *ACS Catal.* **9**, 10253-10259 (2019).

23 Sharafutdinov, I. et al. Intermetallic compounds of Ni and Ga as catalysts for the synthesis of methanol. *J Catal* **320**, 77-88 (2014).

24 Kong, H., Li, H.-Y., Lin, G.-D. & Zhang, H.-B. Pd-Decorated CNT-Promoted $Pd\text{-}Ga_2O_3$ Catalyst for Hydrogenation of $CO_2$ to Methanol. *Catal Letters* **141**, 886 (2011).

25 Bai, S., Shao, Q., Feng, Y., Bu, L. & Huang, X. Highly Efficient Carbon Dioxide Hydrogenation to Methanol Catalyzed by Zigzag Platinum–Cobalt Nanowires. *Small* **13**, 1604311 (2017).

26 Graciani, J. et al. Highly active copper-ceria and copper-ceria-titania catalysts for methanol synthesis from $CO_2$. *Science* **345**, 546-550 (2014).

27 Gong, J. et al. Synthesis of Ethanol via Syngas on $Cu/SiO_2$ Catalysts with Balanced $Cu^0–Cu^+$ Sites. *J Am Chem Soc.* **134**, 13922-13925 (2012).

28 Samson, K. et al. Influence of $ZrO_2$ Structure and Copper Electronic State on Activity of $Cu/ZrO_2$ Catalysts in Methanol Synthesis from $CO_2$. *ACS Catal.* **4**, 3730-3741 (2014).

29 Wang, Y. et al. Insight into the Balancing Effect of Active Cu Species for Hydrogenation of Carbon–Oxygen Bonds. *ACS Catal.* **5**, 6200-6208 (2015).

30 Karelovic, A. & Ruiz, P. The role of copper particle size in low pressure methanol synthesis via $CO_2$ hydrogenation over Cu/ZnO catalysts. *Catal. Sci. Technol.* **5**, 869-881 (2015).

31 Rong, W. et al. Size-Dependent Activity and Selectivity of Atomic-Level Copper Nanoclusters during $CO/CO_2$ Electroreduction. *Angew. Chem. Int. Ed.* **60**, 466-472 (2021).

32 Zhu, Y. et al. Copper-zirconia interfaces in UiO-66 enable selective catalytic hydrogenation of $CO_2$ to methanol. *Nat. Commun.* **11**, 5849 (2020).

33 Witoon, T., Chalorngtham, J., Dumrongbunditkul, P., Chareonpanich, M. & Limtrakul, J. $CO_2$ hydrogenation to methanol over $Cu/ZrO_2$ catalysts: Effects of zirconia phases. *Chem. Eng. J.* **293**, 327-336 (2016).

34 Qiao, B. et al. Single-atom catalysis of CO oxidation using $Pt_1/FeO_x$. *Nat. Chem.* **3**, 634-641 (2011).

35 Nguyen, L. et al. $Ir_1Zn_n$ Bimetallic Site for Efficient Production of Hydrogen from Methanol. *ACS Sustain. Chem. Eng.* **7**, 18793-18800 (2019).

36 Tang, Y. et al. Synergy of Single-Atom $Ni_1$ and $Ru_1$ Sites on $CeO_2$ for Dry Reforming of $CH_4$. *J. Am. Chem. Soc.* **141**, 7283-7293 (2019).

37 Li, H. et al. Synergetic interaction between neighbouring platinum monomers in $CO_2$ hydrogenation. *Nat. Nanotechnol.* **13**, 411-417 (2018).

38 Ye, X. et al. Highly Selective Hydrogenation of $CO_2$ to Ethanol via Designed Bifunctional $Ir_1–In_2O_3$ Single-Atom Catalyst. *J. Am. Chem. Soc.* **142**, 19001-19005 (2020).

39 Han, Z., Tang, C., Wang, J., Li, L. & Li, C. Atomically dispersed $Pt_n^+$ species as highly active sites in $Pt/In_2O_3$ catalysts for methanol synthesis from $CO_2$ hydrogenation. *J. Catal.* **394**, 236-244 (2021).

40 Chen, C. et al. The significant role of oxygen vacancy in $Cu/ZrO_2$ catalyst for enhancing water–gas-shift performance. *Int. J. Hydrog. Energy* **39**, 317-324 (2014).

41 Ikuno, T. et al. Methane Oxidation to Methanol Catalyzed by Cu-Oxo Clusters Stabilized in NU-1000 Metal–Organic Framework. *J Am Chem Soc.* **139**, 10294-10301 (2017).

42 Wang, L.-C. et al. Structural Evolution and Catalytic Properties of Nanostructured $Cu/ZrO_2$ Catalysts Prepared by Oxalate Gel-Coprecipitation Technique. *J. Phys. Chem. C* **111**, 16549-16557 (2007).

43 Velu, S., Suzuki, K., Gopinath, C. S., Yoshida, H. & Hattori, T. XPS, XANES and EXAFS investigations of $CuO/ZnO/Al_2O_3/ZrO_2$ mixed oxide catalysts. *Phys. Chem. Chem. Phys.* **4**, 1990-1999 (2002).

44 Sun, J. et al. Freezing copper as a noble metal–like catalyst for preliminary hydrogenation. *Sci. Adv.* **4**, eaau3275 (2018).

45 Yang, H. et al. Scalable Production of Efficient Single-Atom Copper Decorated Carbon Membranes for $CO_2$ Electroreduction to Methanol. *J. Am. Chem. Soc.* **141**, 12717-12723 (2019).

46 Pang, J. et al. Hierarchical Echinus-like Cu-MFI Catalysts for Ethanol Dehydrogenation. *ACS Catal.* **10**, 13624-13629 (2020).

47 Espinós, J. P. et al. Interface Effects for Cu, CuO, and $Cu_2O$ Deposited on $SiO_2$ and $ZrO_2$. XPS Determination of the Valence State of Copper in $Cu/SiO_2$ and $Cu/ZrO_2$ Catalysts. *J. Phys. Chem. B* **106**, 6921-6929 (2002).

48 Cui, G. et al. $ZrO_2$-x modified Cu nanocatalysts with synergistic catalysis towards carbon-oxygen bond hydrogenation. *Appl. Catal. B* **280**, 119406 (2021).

49 Lamberti, C. et al. XAFS, IR, and UV–Vis Study of the CuI Environment in CuI-ZSM-5. *J. Phys. Chem. B* **101**, 344-360 (1997).

50 Zhang, Z. et al. Transfer Hydrogenation of Fatty Acids on $Cu/ZrO_2$: Demystifying the Role of Carrier Structure and Metal–Support Interface. *ACS Catal.* **10**, 9098-9108 (2020).

51 Gao, J. et al. Cu2In Nanoalloy Enhanced Performance of $Cu/ZrO_2$ Catalysts for the $CO_2$ Hydrogenation to Methanol. *Ind. Eng. Chem. Res.* **59**, 12331-12337 (2020).

52 Zhang, Z. et al. The most active Cu facet for low-temperature water gas shift reaction. *Nat. Commun.* **8**, 488 (2017).

53 Ladera, R. et al. Catalytic valorization of $CO_2$ via methanol synthesis with Ga-promoted Cu–ZnO–$ZrO_2$ catalysts. *Appl. Catal. B* **142-143**, 241-248 (2013).

54 Liu, A. et al. Controlling Dynamic Structural Transformation of Atomically Dispersed $CuO_x$ Species and Influence on Their Catalytic Performances. *ACS Catal.* **9**, 9840-9851 (2019).

55 Andersen, C. W. et al. Redox-Driven Migration of Copper Ions in the Cu-CHA Zeolite as Shown by the In Situ PXRD/XANES Technique. *Angew. Chem. Int. Ed.* **56**, 10367-10372 (2017).

56 Zhang, X. et al. Reaction-driven surface reconstruction of $ZnAl_2O_4$ boosts the methanol selectivity in $CO_2$ catalytic hydrogenation. *Appl. Catal. B* **284**, 119700 (2021).

57 Dandekar, A. & Vannice, M. A. Determination of the Dispersion and Surface Oxidation States of Supported Cu Catalysts. *J Catal* **178**, 621-639 (1998).

58 Pokrovski, K., Jung, K. T. & Bell, A. T. Investigation of CO and $CO_2$ Adsorption on Tetragonal and Monoclinic Zirconia. *Langmuir* **17**, 4297-4303 (2001).

59 Ma, Y. et al. Reactivity of a Zirconia–Copper Inverse Catalyst for $CO_2$ Hydrogenation. *J. Phys. Chem. C* **124**, 22158-22172 (2020).

60 Yang, C. et al. Strong Electronic Oxide–Support Interaction over $In_2O_3/ZrO_2$ for Highly Selective $CO_2$ Hydrogenation to Methanol. *J. Am. Chem. Soc.* **142**, 19523-19531 (2020).

61 Wang, Y. et al. Strong Evidence of the Role of $H_2O$ in Affecting Methanol Selectivity from $CO_2$ Hydrogenation over Cu-ZnO-$ZrO_2$. *Chem* **6**, 419-430 (2020).

62 Wang, J. et al. A highly selective and stable ZnO-$ZrO_2$ solid solution catalyst for $CO_2$ hydrogenation to methanol. *Sci. Adv.* **3**, e1701290 (2017).

63 Li, H. et al. $CO_2$ activation on ultrathin $ZrO_2$ film by $H_2O$ co-adsorption: In situ NAP-XPS and IRAS studies. *Surf Sci* **679**, 139-146 (2019).

64 Soerensen, K. J. & Cant, N. W. Alternating nitrous oxide/reductant cycles and the determination of copper area in supported copper catalysts. *Catal Letters* **33**, 117-125 (1995).

65 Kresse, G. & Furthmüller, J. Efficient iterative schemes for ab initio total-energy calculations using a plane-wave basis set. *Phys. Rev., B Condens. Matter* **54**, 11169-11186 (1996).

66 Blöchl, P. E. Projector augmented-wave method. *Phys. Rev., B Condens. Matter* **50**, 17953-17979 (1994).

67 Kresse, G. & Joubert, D. From ultrasoft pseudopotentials to the projector augmented-wave method. *Phys. Rev. B* **59**, 1758-1775 (1999).

68 Perdew, J. P. & Wang, Y. Accurate and simple analytic representation of the electron-gas correlation energy. *Phys. Rev. B* **45**, 13244-13249 (1992).

69 Huang, S. D., Shang, C., Kang, P. L., Zhang, X. J. & Liu, Z. P. LASP: Fast global potential energy surface exploration. *WIREs Comput. Mol. Sci.*, e1415 (2019).

70 Guan, S. H., Zhang, K. X., Shang, C. & Liu, Z. P. Stability and anion diffusion kinetics of Yttria-stabilized zirconia resolved from machine learning global potential energy surface exploration. *J. Chem. Phys.* **152**, 094703 (2020).

71 Ma, S. C., Shang, C., Wang, C. M. & Liu, Z. P. Thermodynamic rules for zeolite formation from machine learning based global optimization. *Chem. Sci.* **11**, 10113-10118 (2020).

72 Guan, S. H., Shang, C., Huang, S. D. & Liu, Z. P. Two-Stage Solid-Phase Transition of Cubic Ice to Hexagonal Ice: Structural Origin and Kinetics. *J Phys Chem C* **122**, 29009-29016 (2018).

73 Huang, S.-D., Shang, C., Zhang, X.-J. & Liu, Z.-P. Material discovery by combining stochastic surface walking global optimization with a neural network. *Chem. Sci.* **8**, 6327-6337 (2017).

74 Behler, J. & Parrinello, M. Generalized neural-network representation of high-dimensional potential-energy surfaces. *Phys. Rev. Lett.* **98**, 146401 (2007).

# Declarations

Acknowledgements

This work is supported by the National Natural Science Foundation of China under grant Nos. 21902029, 21902027, 51701201 and U19B2003, Natural Science Foundation of Fujian Province under grant Nos. 2020J05121 and 2020J01443, DNL Cooperation Fund, CAS (DNL201903). We thank the staff at the BL14W1 beamline of the Shanghai Synchrotron Radiation Facilities and Dr. Mohsen Shakouri at Canadian Light Source for assistance with the EXAFS and XANES measurements.

Author contribution

Li Tan conceived and designed the experiments. Huibo Zhao performed the catalysts synthesis, characterization and performance experiments. Zhipan Liu and Sicong Ma contributed to the DFT calculation. Ruofan Yu, Yang Chen, Kaizhuang Xu, Yuan Fang, Caixia Zhu, and Xiaochen Liu assisted with the catalysts synthesis and performance test. Yu Tang and Lizhi Wu help analyzed the XPS and XAS data. Qike Jiang conducted the HAADF-STEM experiments. Peng He and Yingquan Wu assisted with the In-Situ DRIFT experiments and $N_2O$ titration experiments. Li Tan and Huibo Zhao wrote the paper.

Competing interests

The authors declare no competing interests.

# Figures

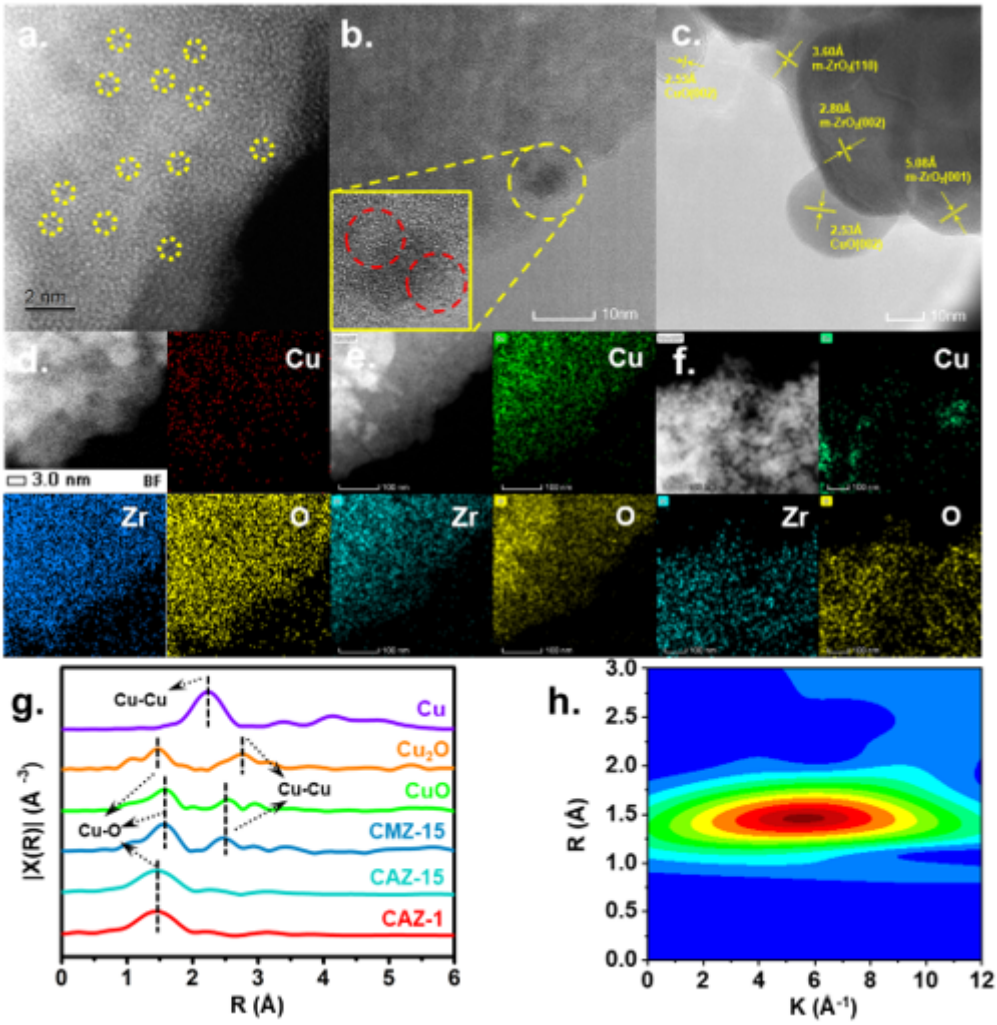


**Figure 1**

HAADF-STEM image and elements mapping of CAZ-1 (a, d), HRTEM and elements mapping of CAZ-15 (b, e), CMZ-15 (c, f). The corresponding k2-weighted Fourier transform spectra of as-prepared samples and references (g). The contour plots of the WT spectra of CAZ-1 (h).

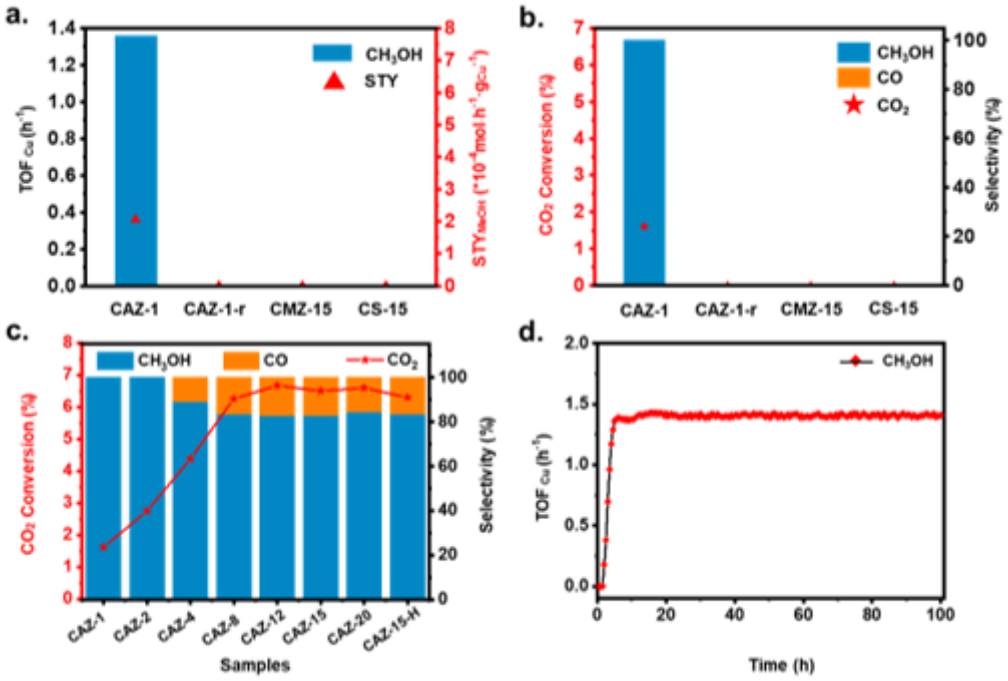


## Figure 2

Catalytic performance of different Cu catalysts. TOFCu values, Space-time yield, CO2 conversion and production selectivity for CAZ-1, CMZ-15 and CS-15 (a, b); The catalytic activity for CAZ-x and CAZ-15-H catalysts (c); The stability test for CAZ-1(d). CAZ-15-H is represented of CAZ-15 pre-treated by HNO3 for 20h. Reaction condition: 3MPa, 180 oC, CO2:H2=1:3, 10mL/min.

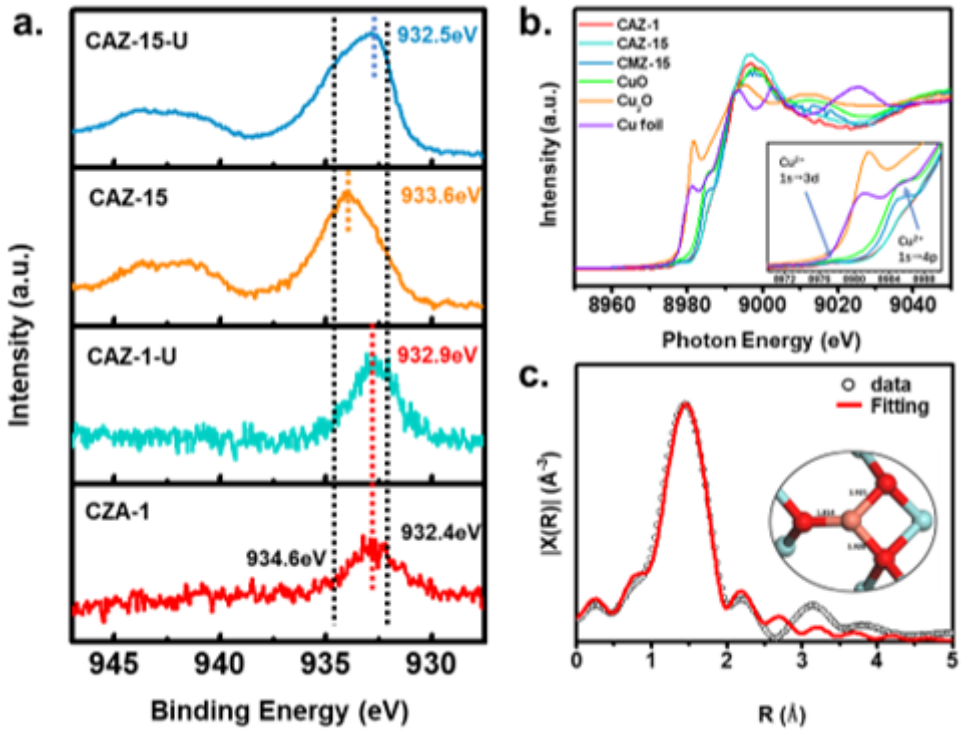


## Figure 3

The surface chemical state and local structure for different Cu/ZrO2 catalysts. XPS spectra of Cu 2p for fresh and used CAZ-1 and CAZ-15 catalyst (a); XANES spectra of CAZ-1, CAZ-15 and CMZ-15 as well as the Cu foil, Cu2O and CuO reference at the Cu k-edge (b); The EXAFS fitting result and geometric structure of CAZ-15 (c). U: used catalysts.

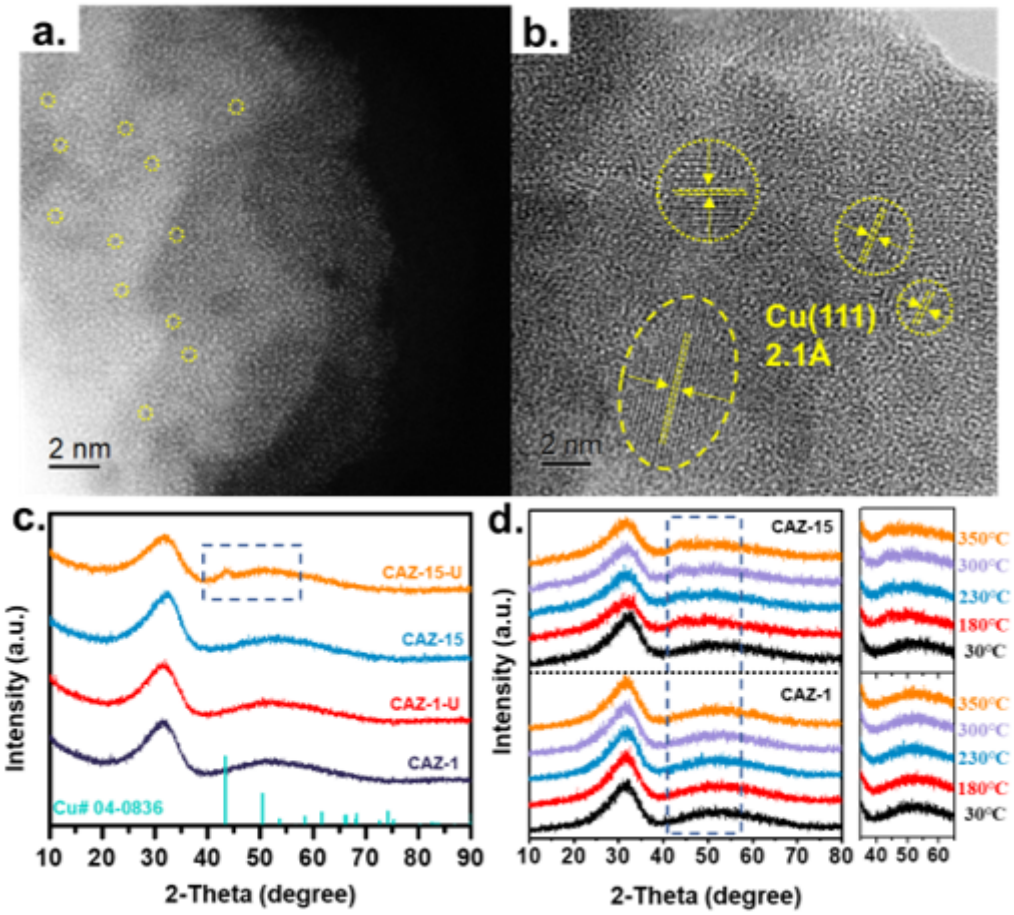


## Figure 4

The morphology and crystal structure for different Cu/a-ZrO2 catalysts. HAADF-STEM of used CAZ-1(a); HRTEM of used CAZ-15 catalyst (b); XRD for fresh and used CAZ-1, CAZ-15 catalysts (c); In-situ XRD for different Cu/a-ZrO2 under pure H2 condition (d). U: used catalyst.

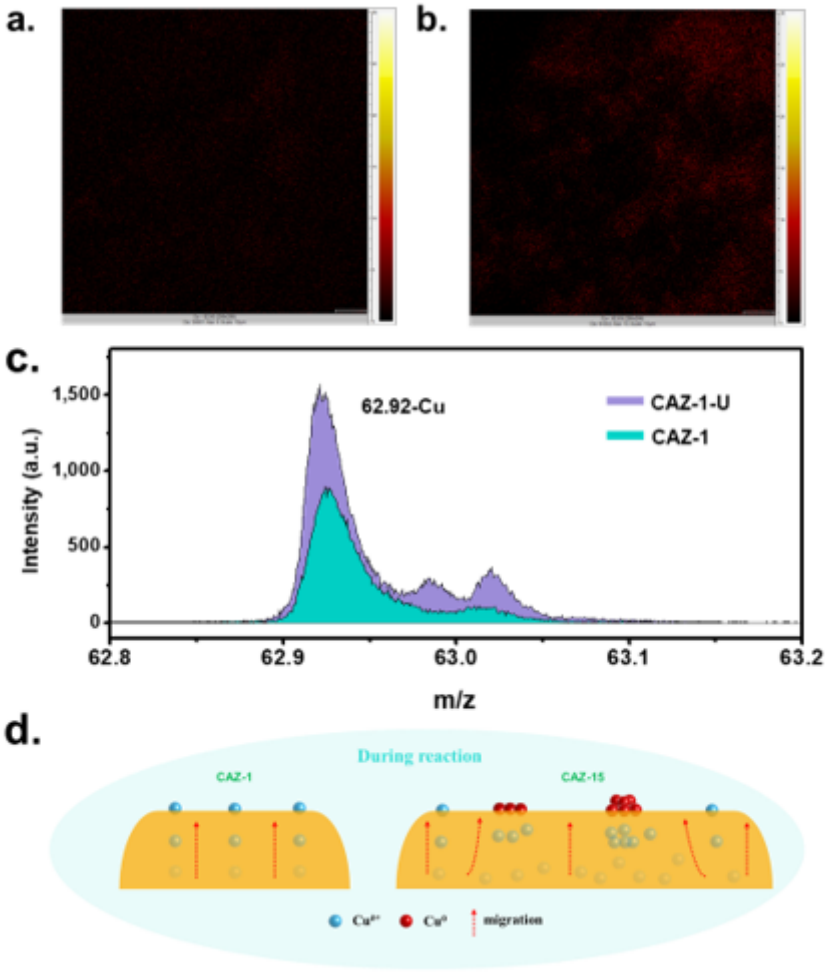


## Figure 5

TOF-SIMS images and spectrum for fresh CAZ-1 and used CAZ-1. Cu mapping for fresh CAZ-1 (a); Cu mapping for used CAZ-1 (b); TOF-SIMS spectra for fresh and used CAZ-1 (c); Schematic diagram of the migration of Cu species for CAZ-1 and CAZ-15 in the hydrogenation reaction (d). Note: the write scale bars represent 10 μm in (a), (b). U: used catalyst.

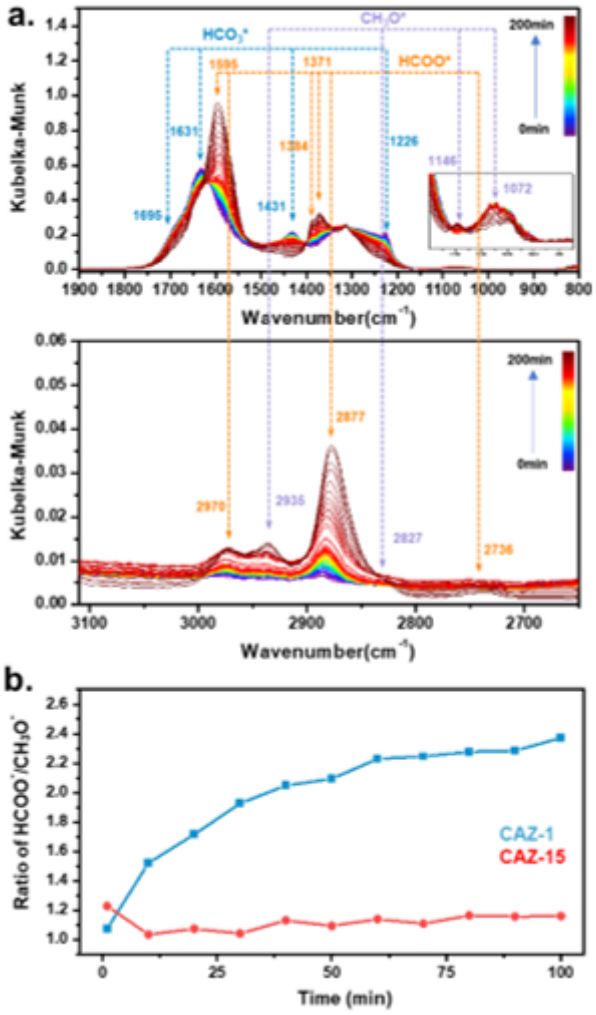


## Figure 6

In-situ DRIFT spectroscopy for CAZ-1. Analysis condition: the sample was first pretreated under Ar atmosphere at 230oC for 60min, then insert CO2+H2 (1:3) to 3MPa and record data at 180oC for 100min.

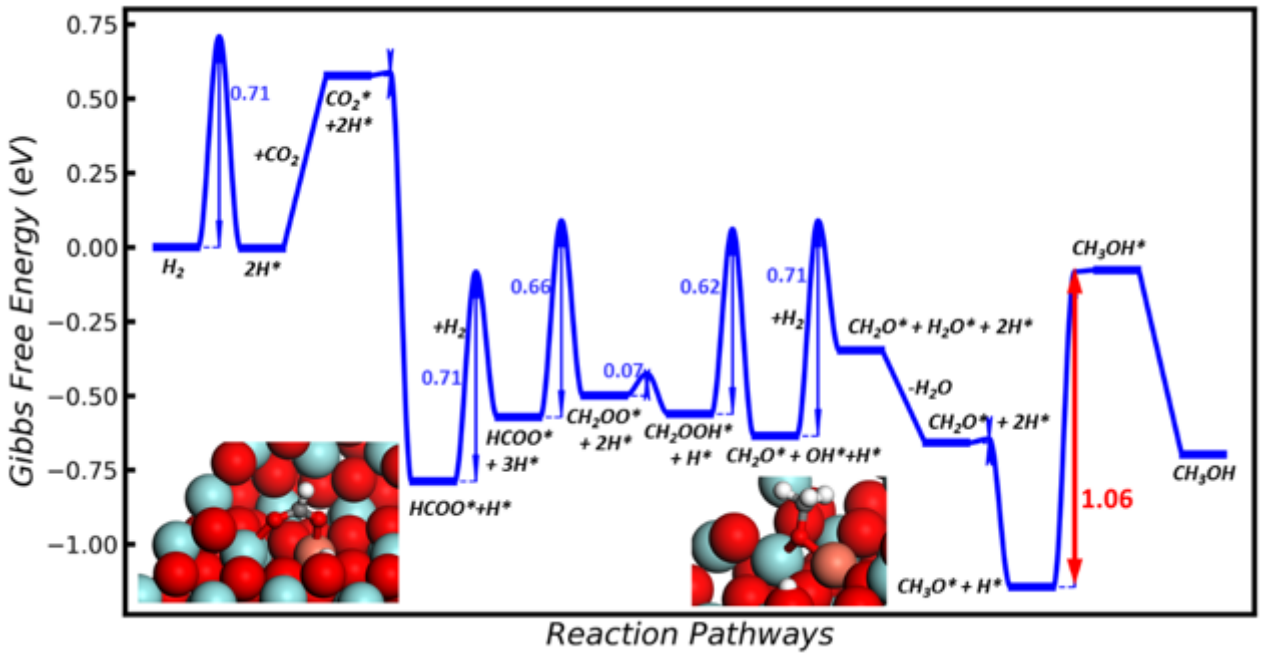


**Figure 7**

Gibbs free energy profile of CO2 hydrogenation to CH3OH on Cu/a-ZrO2 catalysts at 180 oC and 3MPa CO2/H2 gas (CO2:H2 = 1:3). The asterisk indicates the adsorption state. The reaction snapshots are shown with the Cu, Zr, O, C and H in orange, cyan, red, grey and white colors, respectively.

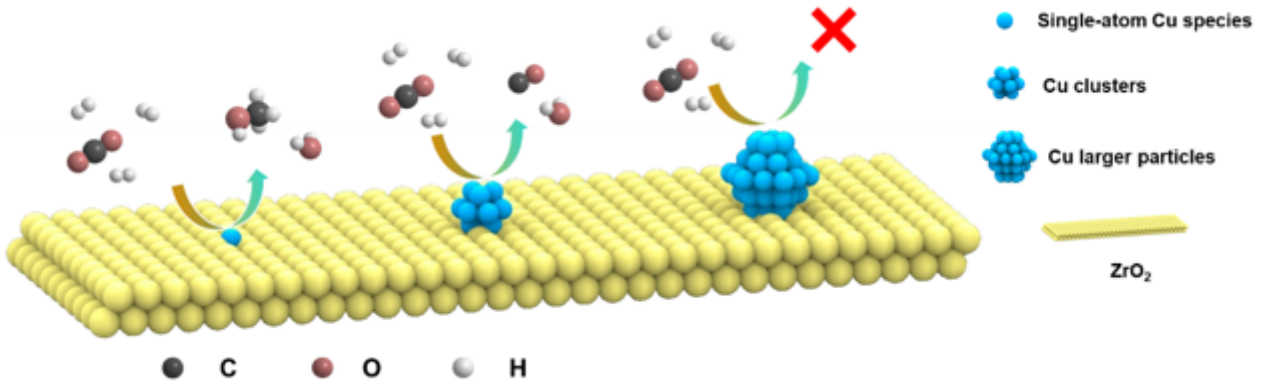


**Figure 8**

The reaction diagram for different Cu-Zr catalysts.

## Supplementary Files

This is a list of supplementary files associated with this preprint. Click to download.

- SupplementaryInformation.pdf